Extreme-Microgap (x-μgap) Based Hotspot Thermal Management with Refrigerant Flow Boiling

Mohamed H. Nasr,[1] Craig E. Green,[1] Peter A. Kottke,[1] Xuchen Zhang,[2] Thomas E. Sarvey,[2] Yogendra K. Joshi,[1] Muhannad S. Bakir,[2] Andrei G. Fedorov[1,*]
[1]George W. Woodruff School of Mechanical Engineering
[2]School of Electrical and Computer Engineering
Georgia Institute of Technology,
Atlanta, GA 30332
*Corresponding Author: AGF@gatech.edu

ABSTRACT

Performance of the next generation microprocessors is rapidly reaching its limits due to inability to remove heat, especially at high power density from so-called local "hotspots". Convective boiling heat transfer in microgap heat sinks has the potential to dissipate ultra-high heat fluxes. We report results of an experimental investigation of heat transfer performance of three dedicated microgap coolers for hotspot thermal management. In this study, a rectangular microgap, batch micromachined in silicon and instrumented with thin-film resistive thermometry, is employed to assess its capability of dissipating extreme heat fluxes of multiple kW/cm^2 while keeping the wall temperature within the limits dictated by electronics reliability. Convective boiling in microgap with heights of 5 μm and 10 μm was tested with and without pin fins in the microgap. The test section was heated from the bottom using resistive heaters and capped with glass to enable visual observation of two-phase flow regimes. Microgap pressure drop and wall temperature measurements, mapped into flow regimes, were obtained with R134a as the coolant, for heat fluxes up to 5 kW/cm^2, mass fluxes up to 7,000 kg/m^{2}s, at maximum pressures up to 1.5 MPa and outlet vapor qualities approaching unity. These experimental parameters constitute extreme values in terms of microgap height (smallest reported to our knowledge), mass fluxes, and heat fluxes. New flow regimes, including vapor plumes, liquid slugs, and ultra-thin wavy liquid film, were observed as a function of increasing heat flux and microgap geometry. Dominant mechanism(s) of two-phase heat transfer responsible for each regime have been postulated based on flow visualization correlated with pressure drop and thermal resistance measurements.

KEY WORDS: Two-phase flow, high heat flux, micro-cooler, heat sink, convective boiling, flow visualization, flow regime, R134a, pressure drop, thermal resistance.

NOMENCLATURE

q''_h Heater Heat flux
R'' Thermal Resistance
ΔT Temperature difference between inlet fluid and heater
G Gravity

INTRODUCTION

Increases in microprocessor power density have created a demand for new cooling techniques capable of dissipating high heat fluxes. Local sites of ultra-high heat generation (>1 kW/cm^2) known as hotspots limit microprocessor performance and reliability due to the excessively high temperatures they generate [1]. Convective flow boiling is an attractive thermal solution for high heat flux removal with potential application for hotspot mitigation. Two-phase cooling offers the advantage of utilizing both latent and sensible heat absorption to remove heat. Advancement in fabrication processes have allowed for practical consideration of microgap/microchannel flow boiling on the back side of an active electronic component [2].

While two phase micro-coolers have been an area of active research, few attempts have been made to characterize the thermal performance of microgap coolers [3-6]. Microgap cooling offers an advantage over microchannels in reducing flow instabilities such as high amplitude pressure oscillations and flow reversals due to lack of fluidic communication between adjacent channels [7-9]. Heat transfer performance in micropocessors is found to be a strong function of dominant flow regime in the micrgoap, where a flow regime describes the form that a simultaneous flow of liquid and vapor take. The primary flow regimes observed in two phase flow through miniature horizontal gaps are: bubble, intermittent, annular and stratified flow [10, 11]. Annular flow was shown to be the most prevalent flow regime in microcooler heat sinks where a thin liquid film covers the top and bottom surfaces of the channel with a vapor core in between [4,11]. In previous studies on two phase micro coolers, annular flow boiling regime was observed to have the best thermal performance with the highest heat transfer coefficient as result of minimal thermal resistance in the liquid film [11, 12].

In this study, the thermal performances of three microfabricated extreme-microgap (x-μgap) coolers for hotspot mitigation are characterized in terms of thermal resistance and pressure drop behavior for varying heat and mass fluxes. Boiling flow regimes are presented and interpreted in terms of the underlying physical principles. The devices tested have gap heights of 5 and 10 μm without and with inline cylindrical micro-pin-fin test section. Heat fluxes up to 5 kW/cm^2 and mass fluxes up to 7,000 kg/m^{2}s are investigated and constitute record high parameters never before observed in literature. Part of the challenge in quantitative performance characterization of microgaps with small heated footprint is the difficulty in measuring heat losses, as the power input to achieve record high heat fluxes is quite small (<3W), while the domain for conduction spreading in the device is large with respect to the device dimensions. These challenges make it difficult to accurately estimate wall temperatures and quantify heat transfer coefficient, quality, and void fraction; therefore the results are reported in terms of overall thermal resistance based on relevant junction and ambient temperatures, which is a

meaningful metric for electronics thermal management applications.

DEVICE OVERVIEW

The first device tested, 'Gen 1', is an empty (no fins) microgap as shown in Fig 1 with inlet and outlet ports that are 200 µm in diameter. The inlet and outlet plenums are 200 µm deep to minimize parasitic pressure drops at the fluid entry/exit domains, while the microgap test section is 300 µm long x 200 µm wide x 5 µm high and is located in the middle of the device with three platinum resistance heaters deposited on the back side. The heaters also serve as resistance temperature detectors (RTDs) for temperature measurement. A 2 µm SiO_2 passivation layer is deposited on the heaters to protect against metal oxidation and to reduce heat losses to the environment through the bottom surface. Pyrex glass seals the top side of the microgap and allows for flow visualization. The inlet and outlet ports, plenums as well as the microgap are etched in silicon using Bosch process with high precision and accuracy afforded by batch microfabrication.

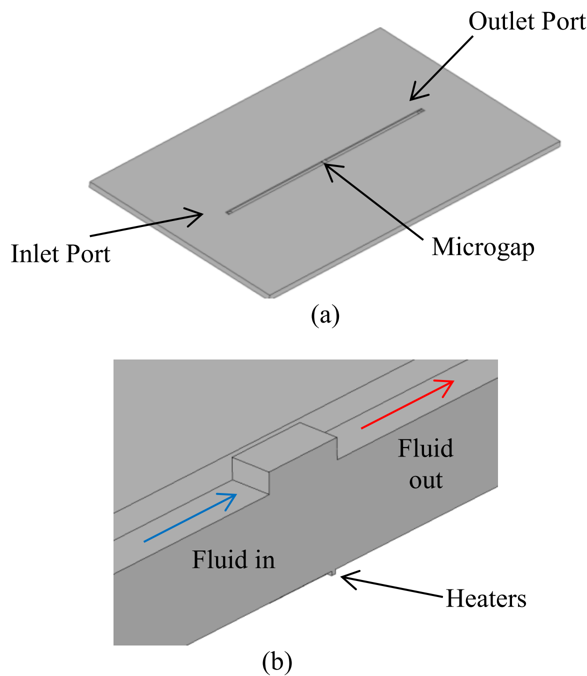

Fig. 1 Gen 1 Device (a) Panoramic view (b) Cross section view at microgap.

The second device, 'Gen 2', is also an empty microgap device similar to Gen 1 and is shown in Fig. 2-b. The microgap footprint is the same, but gap height is now doubled to 10 µm. In addition, the Gen 2 device includes air trenches to reduce conduction heat spreading in the bulk silicon. The air trenches are 40 µm wide and 180 µm tall. The third device characterized, 'Gen 3', contains inline cylindrical pin fins in the 10 µm high microgap that are 4 µm in diameter and 10 µm apart. A cross sectional view of the Gen 3 device is shown in Fig. 2-c and SEM images of the pin fins and heater are shown in Fig. 3. The Gen 3 device contains identical air trenches and heater configuration as the Gen 2 device. Gen 2 and Gen 3 devices employ a single heater protected by 1 µm SiO_2 passivation layer on top. Device features, including air trenches and an array of pin fins are microfabricated using the same Bosch process that was used to create Gen 1 devices.

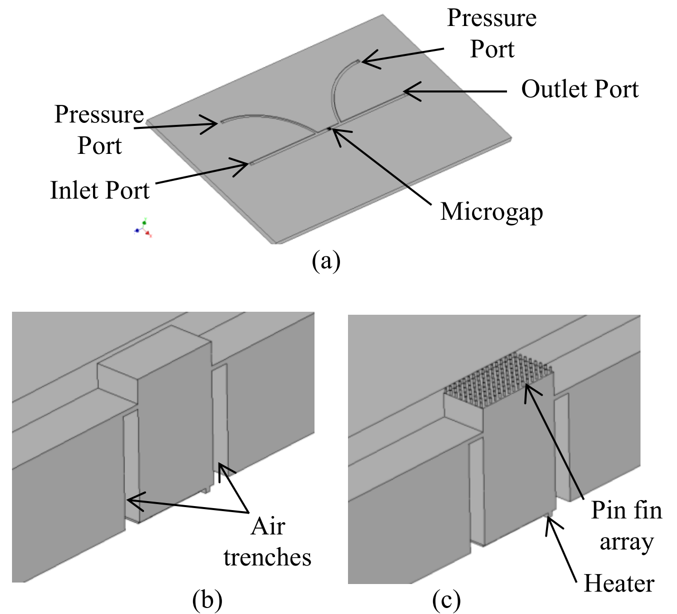

Fig. 2 Gen 2 and Gen 3 Devices: (a) Panoramic view; (b) Gen 2 cross section view; (c) Gen 3 cross section view.

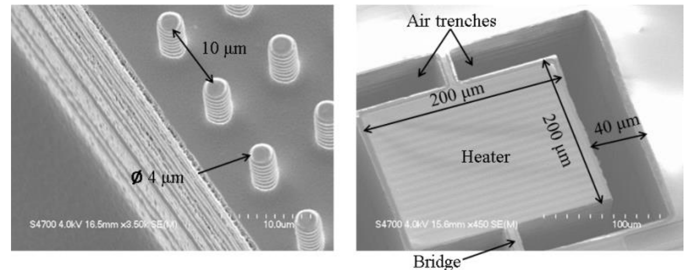

Fig.3 Gen 3 Device SEM Images: (a) Inline pin fins within a microgap; (b) Resistance heater on back side of device (identical in Gen 2 and Gen 3), also showing the air-gap isolation to minimize heat spreading between the heater and an actively-cooled microgap

EXPERIMENTAL SETUP & PROCEDURE

Experimental Setup. The experimental setup used in this study is shown in Fig 4. The devices are housed in a machined PEEK package with O-ring seals for the inlet/ outlet ports and pressure taps (in the case of Gen 2 and Gen 3 devices) as shown in Fig 5. An Agilent 34970a data acquisition unit was used to record pressure drop, heater resistance, circuit current, inlet/outlet fluid temperatures and reservoir temperature for various flow rates across the devices. A KDS Scientific Legato 270 series syringe pump was used to drive refrigerant through the test section at a prescribed flow rate. Fluid temperature measurements were obtained with Omega K-type thermocouples. Pressure drop was measured with Omega PX 309 series pressure transducers. Power was supplied to the device heaters with an Agilent E3641A power source. A fan cooled WBA series thermoelectric was used to condense

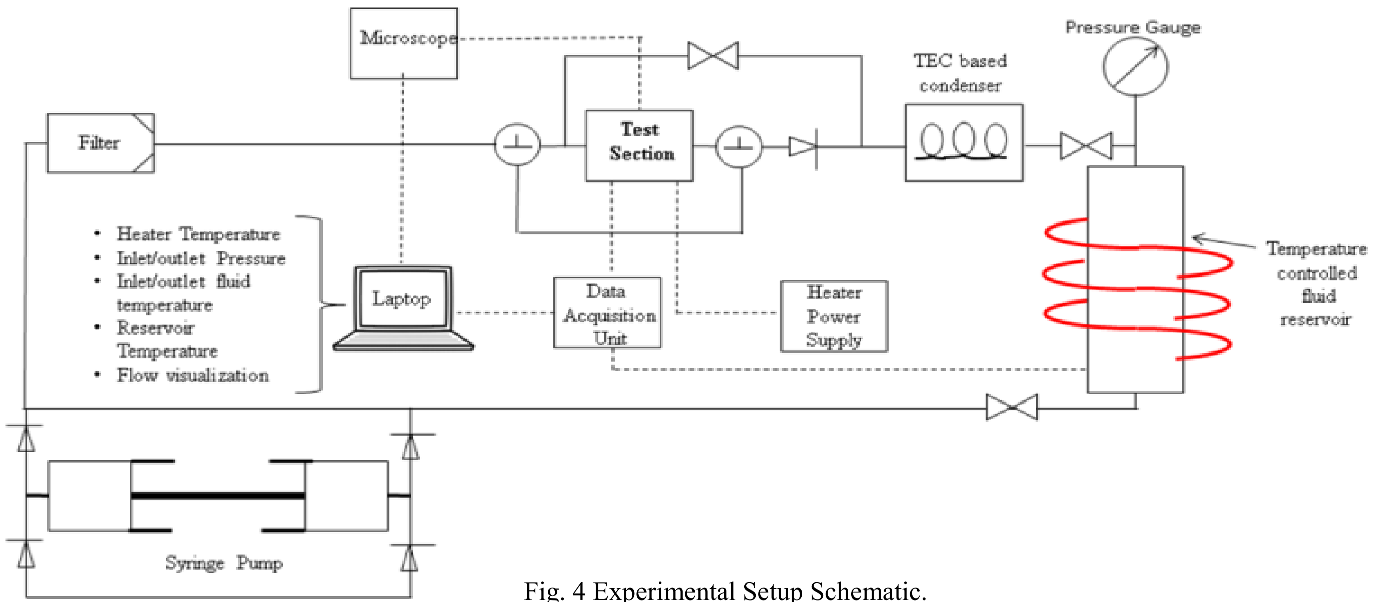

Fig. 4 Experimental Setup Schematic.

vapor coming out of the test section. The reservoir tank was heated by electrical wire heaters with an Omega CN4000 PID controller to drive refrigerant into the system. A Keyence VH-Z100R microscope was used to obtain flow visualization images and videos. Microscope flow visualization images show a top-down view of the microgap test section as shown in Fig 5.

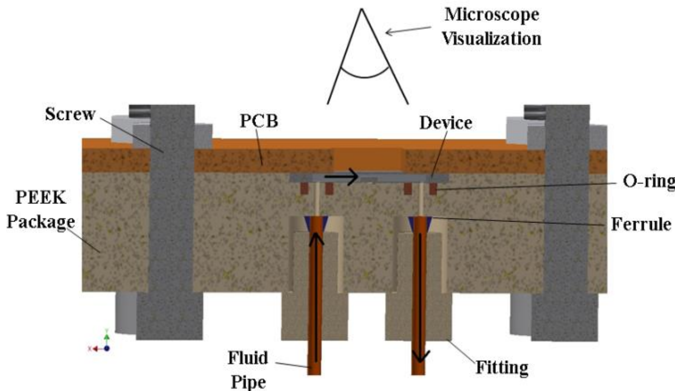

Fig. 5 Cross Section View of Test Section and Hermetic Package. Flow visualization obtained from a top-down view of the microgap with microscope.

Test Procedure. Before starting experiments, device heaters are calibrated in a temperature controlled vacuum oven, showing excellent linear correlation between the RTD resistance and temperature. Experiments started by evacuating the experimental setup to remove most of residual air in the system and charging with R134a. The reservoir tank, containing refrigerant, was pressurized with wire heaters to ensure complete filling of the experimental loop with liquid. Mass fluxes between 1,000 and 7,000 kg/m^{2}s were tested by setting the syringe pump to the desired flow rate and subcooled R134a was delivered to the test device at 22.4°C inlet temperature for all experiments. Power was applied to the heaters in 0.1-0.25W increments until steady state temperatures and pressures were obtained. Flow visualization was performed by microscope with up to 700X lens magnification and continuous video capture with 0.067s time resolution. Power to the heaters was turned off when local dryout was observed in the microgap or when inlet pressure started to approach glass syringe limits to avoid catastrophic failure.

Uncertainties. Error of K-type thermocouple used for heater calibration is +/-0.9°C, error in power applied to heaters from Agilent E3641A power source is +/-0.011W, error in mass flow rate from syringe pump is +/-0.01 mL/s, and error in pressure transducer measurements is +/- 8.62 kPa. Error in microgap height, air trench depth, and pin fin height is within +/- 5% of reported dimensions, and error in heater length and width is within +/- 1% of reported dimensions. Error propagation was applied to assess the uncertainty in mass flux, heat flux and thermal resistance which are found to be +/6.5%, +/- 1.5% and +/-1.7%, respectively.

RESULTS & DISCUSSION

Gen 1 Device. The average thermal resistance, calculated using Eq. 1, of the Gen 1 device as a function of heater heat flux for various mass fluxes is shown in Fig 6. Eq. 1is given by,

$$R'' = \Delta T / q''_h \tag{1}$$

where R'' is the overall device thermal resistance, which includes forced convective boiling of coolant and parallel path of conduction spreading through device silicon, with eventual heat rejection to the environment by radiation and free convection at exposed surfaces of the package. Relevant temperature difference ΔT is between heater/RTD surface and ambient air, and q''_h is the heat flux computed based on supplied power and the area occupied by the resistance heater (200 μm x 200 μm). Total device thermal resistance is used to present thermal performance rather than microgap convective thermal resistance because of the difficulty in quantifying heat flow into the microgap, which will be further discussed at the end of this section. The results on each plot are grouped based on the dominant flow regime in the microgap from flow

visualization. The observed flow regimes for the Gen 1 device are stratified, vapor slug, and ultra-thin liquid film (UTF) boiling. The flow visualization images show a top-down view of the microgap with flow going from left to right. Flow visualization images and cross-sectional schematic interpretation of the flow regimes are shown in Fig 7.

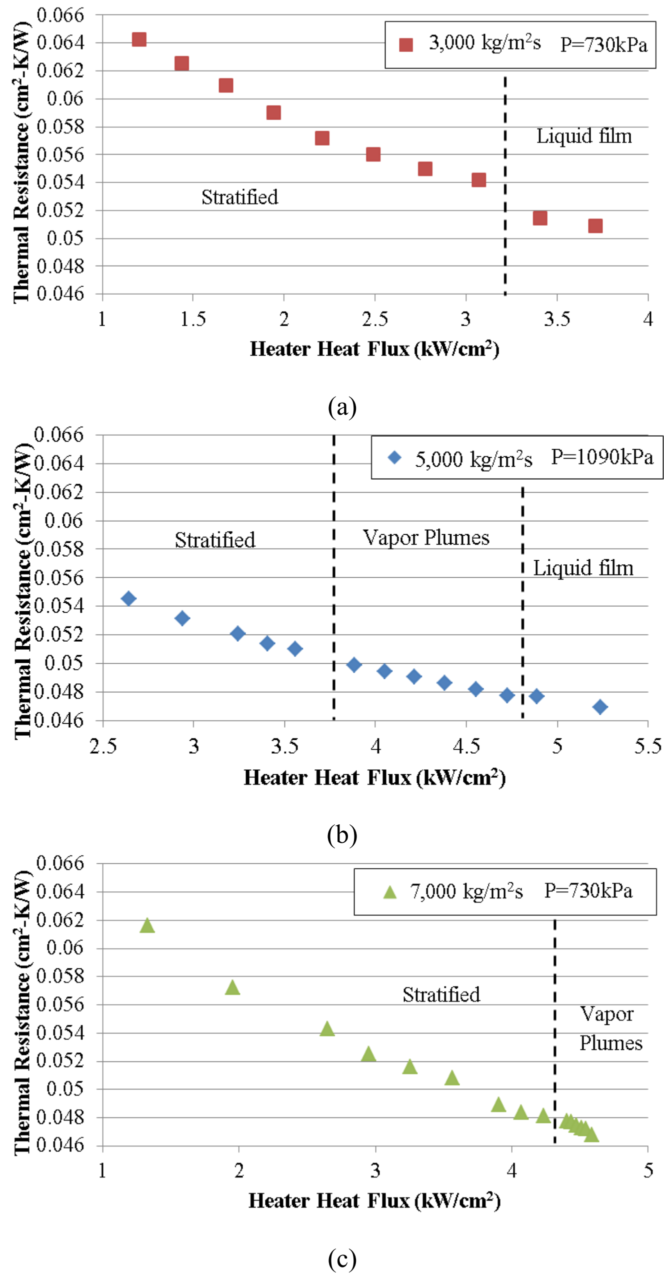

Fig. 6 Thermal Resistance vs Heat Flux for Gen1 Device: (a) G=3,000 kg/m^{2}s (b) G=5,000 kg/m^{2}s (c) G=7,000kg/m^{2}s, mapped into flow regimes described in Fig. 7.

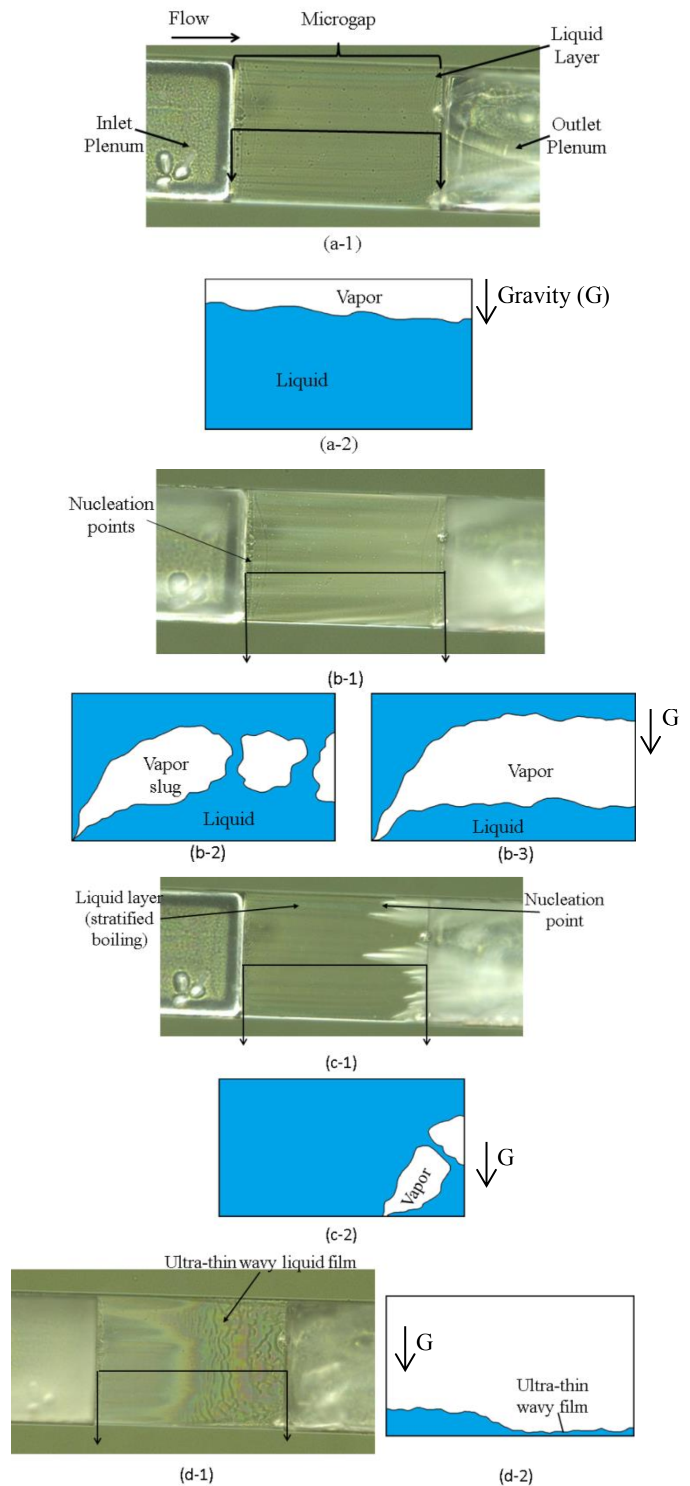

Fig. 7 Boiling Flow Regime Visualization in Gen 1 Device with Schematic Interpretation: (a) Stratified flow (b) Vapor slug flow at low mass fluxes (c) Vapor plume flow at high mass fluxes (d) Ultra-thin wavy liquid film flow.

The stratified flow regime shown in Fig. 7-a-1 was observed at the lowest heat fluxes and consists of a liquid layer on the bottom surface of the channel with a thin vapor layer above as illustrated in Fig 7-a-2. This stratified regime is consistently observed at low heat fluxes for all mass fluxes tested and is initiated at subcooled nucleation sites in the inlet

plenum where vapor is formed and advected into the microgap by the liquid flow. The vapor plume flow regime shown in Fig 7-b and c forms at nucleation points and consists of elongated plumes or slugs that may either be large enough to span the entire microgap or be shorter in length than the microgap but moving so fast that they appear to span the entire microgap (imaging artifacts due to aliasing). Both possible scenarios are shown in the cross section illustrations, Fig 7-b-2 and 7-b-3. The latter interpretation is proposed because the vapor velocities for these experiments are on the order of 1000m/s for mass fluxes beyond 4,000 kg/m^2s, as the vapor density of R134a is 4.25 kg/m^3, while microscope frame rate is too low to capture vapor slug boundaries at that speed. The vapor plume flow regime was observed for middle to highest input heat fluxes tested. At mass fluxes up to 5,000 kg/m^2s, the stratified boiling domain transitions directly to UTF boiling regime with an increase in heat flux. Interestingly, if heat flux is incrementally reduced at the UTF boiling regime, vapor plume boiling becomes dominant as shown in Fig 7-b. This is an embodiment of boiling hysteresis where at a given heat flux boiling may either be in stratified regime or vapor slug regime depending on the sequence of incremental heat input. In contrast, the transition to vapor slug regime at the highest mass fluxes (> 6,000 kg/m^2s) occurs when nucleation points are observed near the outlet of the microgap as shown in Fig. 7-c. As input heat flux is increased, these nucleation points increase in density and move closer to the microgap inlet until the vapor slug flow covers the entire microgap. The inlet conditions at the entry to microgap where liquid is subcooled corroborate the observation of a nucleation front that starts near the outlet of the microgap and moves towards the inlet with increasing heat flux. Single phase liquid entering the microgap is being heated until it reaches saturation temperature, at which point a nucleation front is observed. The extent of single phase flow in the microgap decreases as the heat flux is increased because the fluid reaches saturation temperature more rapidly; this manifests in gradual movement of the nucleation front upstream with an increase in applied heat flux. The difference in transition behavior is a result of the relative impact of an incremental increase in the applied heat flux. For the case of low mass fluxes, fluid within a microgap boils nearly instantaneously even at modest (single increment) increase in the heat flux thus moving the nucleation front from the exit to the inlet of the test section almost immediately and 'bypassing' the vapor plume regime.

The most intriguing flow regime observed for this device is ultra-thin film (UTF) boiling as shown in Fig 7-d. UTF boiling was observed at the highest input heat fluxes and consists of an ultra-thin wavy liquid layer with vapor above. The liquid film is thin enough to reflect light on the order of wavelength equal to its thickness causing an appearance of different colors in flow visualization. A pattern of changing colors in the thin wave region is dynamic and indicative of traveling liquid waves subjected to high velocity vapor flow on top of the layer. There appears to be a reflected color gradient that transition from yellowish/purple to green downstream from the transition point, suggesting a rapid rather than gradual thinning of the liquid layer forming an ultra-thin film with thickness on the order of 400-600 nm. There appears to be no local dryout in this flow regime as indicated by the continuous decrease in the thermal resistance for increased heat fluxes (Fig. 6), whereas thermal resistance can be seen to approach a minimum and begin to increase in Gen 2 and 3 devices upon reaching local dryout (Fig. 12).

Gas assisted thin film evaporative cooling studies in miniature channels [12-14] showed similar physical behavior with observed UTF boiling regime. The underlying driving forces that dominate gas assisted thin film flow dynamics are tangential stresses at the gas-liquid interface and thermocapillary effects resulting from surface temperature gradient along the gas liquid interface [14]. The thermocapillary effect makes heat and mass travel towards areas of high surface tension, which is a function of temperature. Friction between gas and liquid layers accelerates and stabilizes the thin liquid film [13], however thermocapillary effect plays a more significant role in causing wave perturbations [14]. These phenomena are in agreement with qualitative observations in Gen1 device. The liquid film velocity in UTF boiling regime is found to be larger than that of stratified boiling regime, suggesting that there is acceleration in liquid flow by the vapor and thereby enhanced heat transfer properties. The varying ultra-thin film thickness, or wave perturbations, observed as patterns of reflected colors in Fig 7-d are consistent with presence of thermocapillary surface waves at the vapor-liquid interface. In addition, the difference in velocity between vapor and liquid phase is expected to contribute to the tangential stresses at the phase interface which cause wave structure formation via pressure differential in fluid vortexes following the Kelvin-Helmholtz instability.

UTF boiling was reported by Ohadi and co-workers to be one of the most effective methods of high heat flux removal because of the unparalleled high heat transfer coefficients, low quantity of fluid required to wet surface, and small temperature rise of surface above saturation temperature of fluid [15]. Similarly, in our experiments thermal resistance plots as a function of heater heat flux in Fig 6 show steadily declining thermal resistance with increases in heat flux suggesting improved heat removal performance. As mass flux was increased, flow regime transitions occurred at higher heat fluxes and thermal resistances decreased as expected with higher heat removal rates.

Thermal resistance trends did not show noticeable change at flow regime transitions because of significant conduction heat spreading that occurs in the Gen1 device, however the general trend of decreasing thermal resistance with increasing heat flux is consistent with observed transitions in boiling regimes of increasing vapor content in the absence of local dryout [2,10]. The 280 μm thick silicon base of the device, surrounding the small heated area of the hotspot, introduces an additional path for heat flow from the heater to the ambient bypassing microgap. The ability for heat flow to bypass the microgap by conduction through silicon does not allow for direct correlation of the thermal data (temperature and heat flux) obtained at the heaters and convective boiling in the microgap to be able to produce meaningful predictions of heat transfer coefficient for convective boiling. Likewise, estimates of quality cannot be performed as they require accurate

knowledge of heat losses to compute heat input to the fluid. Void fractions also cannot be accurately estimated from flow visualization because the across-the-gap distribution of liquid and vapor in the microgap cross section is difficult to establish from top-down visualization, particularly with the high vapor velocities which appear as streaks shown in Fig 7-b and Fig 7-c. Due to a relatively large medium for conduction heat spreading and small heat input needed to achieve highest heater heat fluxes (<3W), traditional methods of experimentally estimating heat losses such as correlating heat losses to heater temperature are ineffective. Furthermore, use of energy balance for single phase flow to assess heat losses is not possible because of challenges in accurate measurements of the coolant temperature increase from inlet and outlet due to impossibility of bringing thermocouples in direct proximity of the microgap inlet/outlet. Heat losses are reduced in the Gen 2 and Gen 3 devices by etching air trenches around the heaters to direct heat flow to the microgap, as shown in Fig 8b. However, there is still non-negligible heat spreading to the silicon bulk through the bridges holding the hotspot domain in place, as shown in Fig 3. With large uncertainty in heat loss estimates, quality and void fraction are not reported in this study.

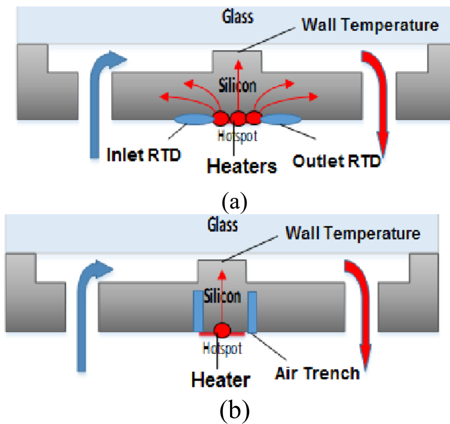

Fig. 8 Air Trench Isolation Effect on Conduction Heat Spreading: (a) Gen 1 device has no air trench and heat supplied at the bottom of the test structure is able to spread throughout silicon; (b) Gen 2 and 3 devices use an air trench to reduce heat conduction spreading and to direct a greater fraction of the heat supply to the microgap.

Gen2 Device. Thermal resistance as a function of heat flux at the heater surface in the Gen 2 devices for various mass fluxes is shown in Fig. 9. Flow visualizations supplemented by illustrated interpretations of the boiling regimes for high and low mass fluxes are presented in Fig. 10 and 11, respectively. The dominant flow regimes from flow visualization are vapor plume, liquid slug, and liquid film boiling, which are mapped to domains that show change in trends of thermal resistance variation. The nucleation sites in the microgap inlet plenum that generated the stratified flow regime in Gen1 devices were not observed in Gen 2 devices. Nucleation in the inlet plenum prior to boiling in the microgap may have sensitivity to the surface features of the plenum as it was observed in some Gen1 and Gen 3 devices. Overall, nucleation in the inlet plenum has a negligible impact on thermal resistance of the device and pressure drop as the coolant is primarily in liquid phase. Vapor plume boiling in the Gen 2 devices takes the same form as that observed in the Gen 1 device; at low mass fluxes (<2000 kg/m^{2}s) boiling transitions from the outlet plenum directly to the inlet plenum with vapor slugs spanning the entire length of the microgap as shown in Fig 11-b. At high mass fluxes (≥2000 kg/m^{2}s) the nucleation points emerge near the outlet of the microgap and move in the direction opposing flow as heat flux is increased. The vapor plume forms a curved front because fluid in the microgap rejects heat to the side walls, which are expected to be at a lower temperature than the saturated fluid because the air trenches provide a significant thermal barrier for heat flow to the side walls as shown in Fig 3.

The decrease in single phase thermal resistance in Fig 9 is not due to particularities of the microgap flow, but an artifact of heat flow path through the device. Thermal resistance of the device was found to decrease in the absence of coolant at low heat fluxes up to 1.40 kW/cm^2 as the heat transfer by natural convection improved with an increase in the glass surface temperature. Beyond 1.40 kW/cm^2 device thermal resistance remained constant as the resistance to heat transfer by convection at the glass surface was reduced to the level of being no longer dominant in the total thermal resistance of the device. Thus, at low heat fluxes single phase coolant flow thermal resistance is approximately constant as expected for fully developed flow, and the observed trend of decreasing total resistance is due to higher heat rejection rates through the glass surface. At higher heat fluxes, the transition from liquid to vapor plume regime caused thermal resistance to decrease with increases in vapor void fraction due to enhanced evaporation rate via thinning of the liquid layer on the heated surface of the microgap.

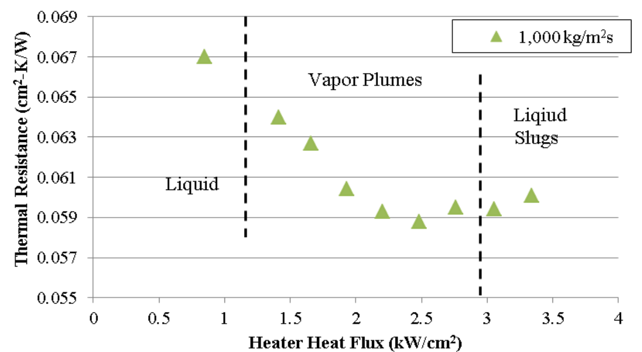

(a)

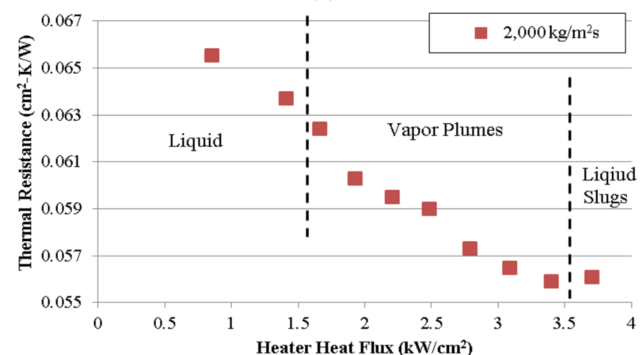

(b)

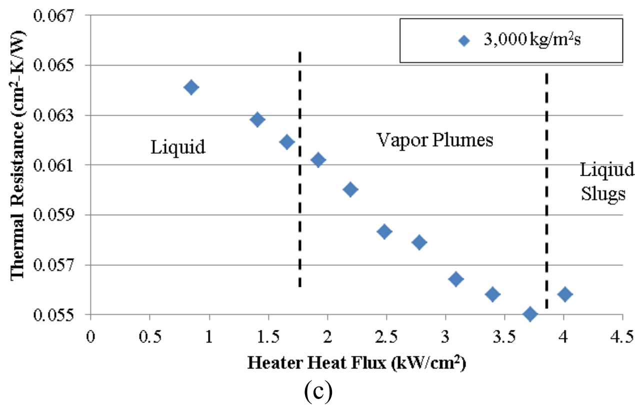

(c)

Fig. 9 Thermal Resistance vs applied heat flux for Gen 2 device: (a) G=1,000 kg/m^2s (b) G=2,000 kg/m^2s (c) G=3,000kg/m^2s, mapped into flow regimes described in Fig. 10.

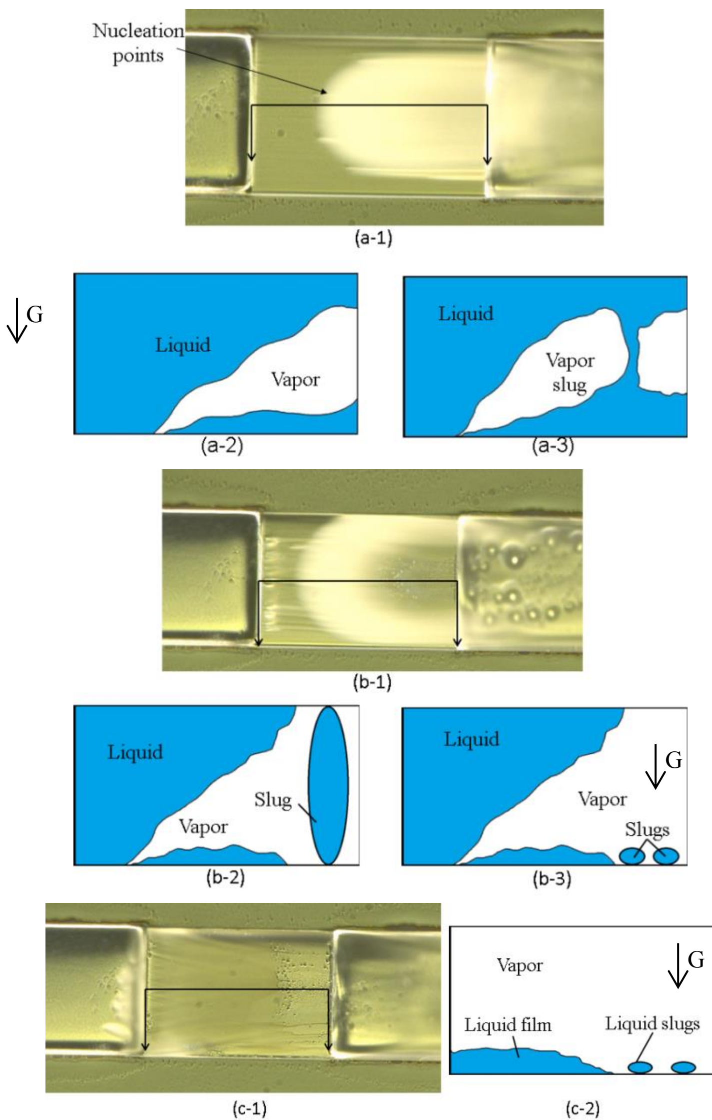

Fig. 10 Boiling Flow Visualization in Gen 2 Device at 3,000 kg/m^2s with cross sectional schematics of flow regime interpretation: (a) Vapor plume flow; (b) Liquid slugs flow; (c) Liquid film flow.

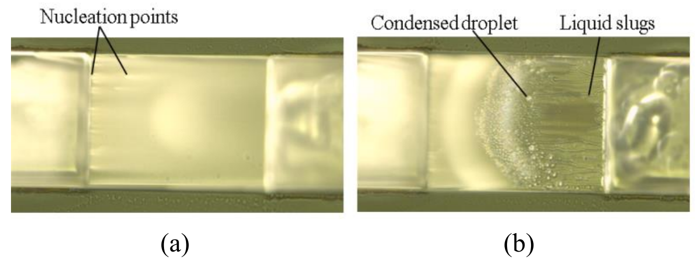

(a) (b)

Fig. 11 Boiling Flow Visualization in Gen 2 Device mass fluxes <3000 kg/m^2s, showing (a) vapor plume boiling spans the entire microgap as nucleation points emerge in the inlet plenum; (b) transition of vapor slug boiling directly to liquid slugs with condensation on glass surface is observed without an intermediate regime of thin film regime.

As heat flux is increased, the two-phase flow regime transitions to liquid slug boiling for low mass fluxes and liquid film boiling for high mass fluxes. At low mass fluxes the liquid layer beneath the vapor slugs gets thinner until the heated gap surface becomes partially dry and liquid slugs are pushed across as shown in Fig 11-b. Since the flow visualization images show a top-down view, the height of the slugs may be as tall as the gap height or smaller; both possibilities are illustrated in Fig 10-b-2 and 10-b-3. Furthermore, residual (condensed) liquid droplets appear on the glass surface supporting the interpretation that there was a liquid film on the glass side (top surface) of the microgap. At high mass fluxes, a thin liquid film was observed before it broke up into liquid slugs. Capillary cohesion forces are suspected to play the main role in keeping the film intact.

Heat transfer performance degraded at liquid slug/ film boiling as result of the local dryout. Thermal resistance reached a minimum value and gradually started to increase as shown in Fig 9. At this transition to local dryout, the device heater started to degrade and higher heat flux data was not collected to maintain an accurate heater calibration. The ability to detect transitions in thermal performance as a function of different boiling regimes suggests that the air trenches do limit conduction spreading in the bulk silicon as Fig. 8 suggests. Heat spreading through the heater bridges between the air trenches shown in Fig. 3 for Gen 2 and Gen 3 devices may still contribute significant losses due to the low power output of the heaters, therefore quality and vapor fraction cannot be accurately estimated though energy balance calculations.

Gen 3 Device. Thermal resistance as a function of heater heat flux for Gen 3 devices at various mass fluxes is presented in Fig 12. The dominant boiling regimes follow those of Gen 2 devices and include vapor plume boiling and liquid slug boiling. Representative flow visualization images of these boiling regimes are presented in Fig. 13. The illustrated interpretations are similar to those shown for the same regimes observed in the Gen 2 devices. No differences in flow regime transition or behavior between low and high mass fluxes were observed in the Gen 3 device, likely because of the presence of fins which disrupt the flow patterns and homogenize the flow structure regardless of the magnitude of mass flux. Vapor slugs and liquid slugs appear in a parabolic pattern with more

boiling near the side walls and less in the middle of the microgap, differing from Gen 2 devices which showed more boiling in the center. Increased hydrodynamic resistance near the side walls resulting from tighter spacing of the pin fins results in locally lower flow rates at the side wall and therefore more boiling. It is difficult to assess whether a liquid film regime exists at high mass fluxes due to the small spacing between the fins, which prevents detailed optical visualization.

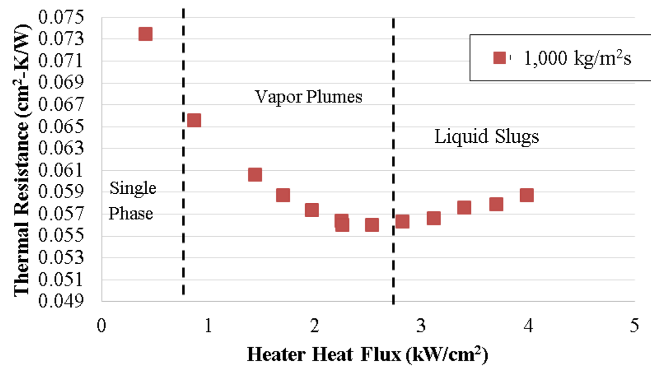

(a)

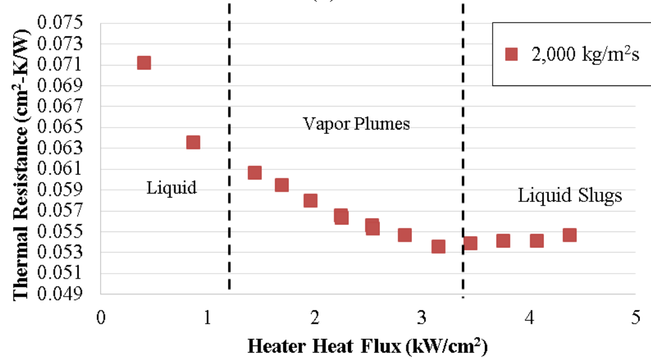

(b)

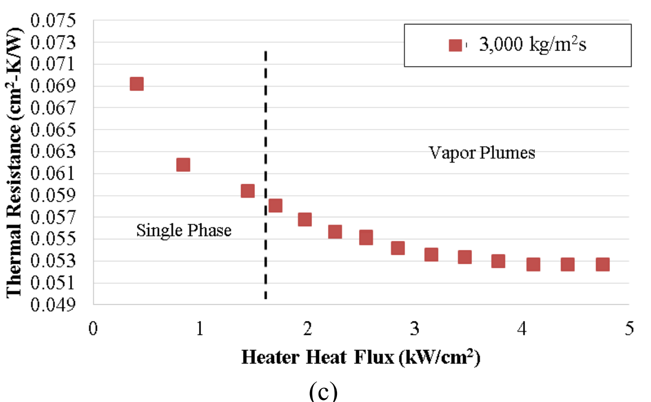

(c)

Fig. 12 Thermal Resistance vs heat flux for Gen 3 device: (a) G=1000 kg/m^2s (b) G=2000 kg/m^2s (c) G=3000 kg/m^2s, mapped into flow regimes described in Fig. 13.

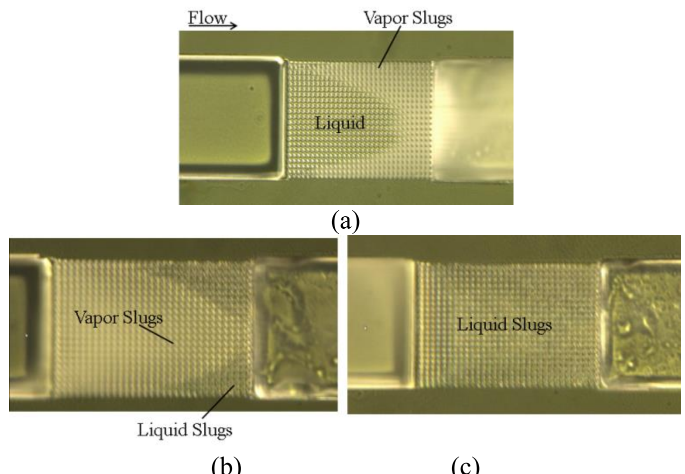

Fig. 13 Visualization of Gen 3 device flow regimes: (a) vapor plume flow, (b) transition to liquid slugs flow, (c) liquid slug flow

Thermal resistance trends in the Gen 3 devices follow similar trends as those in the Gen 2 device, with decreasing thermal resistance during vapor plume boiling due to decreasing liquid layer thickness and increasing thermal resistance during liquid slug boiling due to increasing area of dry patches. The pin fins in Gen 3 devices increased surface area contact with the coolant in the microgap by a factor 2.27, which resulted in a reduction of the minimal overall thermal resistance of Gen 3 devices by an average of 3.5% compared to Gen 2 devices. While the pin fins greatly enhanced the contact area for heat rejection to the coolant, they also disrupted the continuity of the liquid film wetting the microgap surface, which is responsible for the highest heat removal rates in convective boiling [4,11,15]. With a high pin fin density in Gen 3 devices, recirculation zones behind the fins may cause an increase in thermal resistance if slow moving fluid rapidly evaporates in these zones. This is expected to be the case for tests done at 1,000 kg/m^2s and 2,000 kg/m^2s where flow regime transitions in the microgap occur at similar heat fluxes for Gen 2 and Gen 3 devices. It was expected that the increase in inlet pressure resulting from flow constriction in the presence of pin fins would raise the saturation temperature of the coolant in Gen 3 devices thereby shifting flow regime transitions to higher heat fluxes than Gen 2 devices. This was observed in the 3,000kg/m^2s test, where the transition to liquid slug regime in Gen 2 devices was observed at 3.71kW/cm^2 and not in Gen 3 devices even at heat fluxes as high as 4.75kW/cm^2, where the fluid remained in the vapor plume regime. Although Gen 3 devices did not greatly reduce thermal resistance when compared to Gen 2 devices, they can extend the range of operation at low thermal resistance to substantially higher heat fluxes where the thermal performance of Gen 2 devices would degrade.

Repeated tests at the same heat and mass fluxes on multiple Gen 3 devices showed consistent boiling mechanism and thermal performance; however, there were some outlying observations that are not well understood, but worth mentioning. One device tested showed a bubbly flow regime at low heat fluxes, for which in other Gen 3 devices single

phase flow was observed. These bubbles were generated at nucleation sites in the inlet plenum and advected into the microgap by the bulk liquid flow. This behavior was similar to the stratified boiling regime of Gen 1 device shown in Fig 7-a. The emergence of stratified flow in Gen 1 devices and bubbly flow in Gen 3 devices may be related to the surface roughness of the inlet plenum, which may contribute to nucleation in some devices and not others. As heat flux was increased in the bubbly flow regime, the density of bubbles increased resulting in bubble coalescence in the outlet plenum. Rather than transition to a vapor plume regime as typically observed in other devices, the zone of the bubbly flow expanded to a point where the entire microgap dried out momentarily followed by rewetting of the surface and finally stable liquid slug flow. When the heat flux was reduced following the onset of liquid slug boiling, the vapor plume regime was recovered. This boiling hysteresis was repeatable and occurred consistently in several tests of the same device. The boiling hysteresis where bubbly flow regime 'bypassed' the vapor plume regime as heat fluxes were increased occurred after running a few tests in reverse flow. This suggests that there could have been trapped vapor bubbles in the system that were introduced into the device, which would explain the brief dryout in the microgap prior to rewetting.

Pressure Drop. Pressure drop as a function of heater heat flux for all devices tested at various mass fluxes is shown in Fig. 14. The Gen1 device shows nearly uniform pressure drop in the stratified boiling regime with increases in heat flux across a wide range of mass fluxes. The vapor fractions in stratified boiling regime appear to be very low in flow visualization as shown in Fig. 7a with flow being primarily in liquid phase. This is supported by a constant pressure drop at heat fluxes in the stratified flow regime. The transition to vapor slug boiling increased total pressure drop due to the addition of an acceleration pressure drop between vapor and liquid phases. Pressure drop continues to increase with increases in vapor content at higher heat fluxes in the vapor plume regime (Fig. 7-b-c); when vapor slugs occupy the entire microgap, the pressure drop is nearly double that of the stratified boiling regime. The large pressure drop particularly occurs when boiling transitions to the inlet plenum, which substantially raises the inlet pressure. This could be due to numerous factors, but most likely due an increased pressure head loss due to rapid constriction at the inlet when fluid enters a microgap at high velocity as vapor-rich two-phase mixture. The outlet pressure is always fixed at the system pressure due to the presence of a large buffering reservoir filled with a refrigerant's saturated mixture at a fixed temperature, so the change in inlet pressure directly correlates with the pressure drop. The transition to UTF boiling (Fig 7-d) showed a small increase in pressure drop from that of vapor slug boiling as vapor content increased.

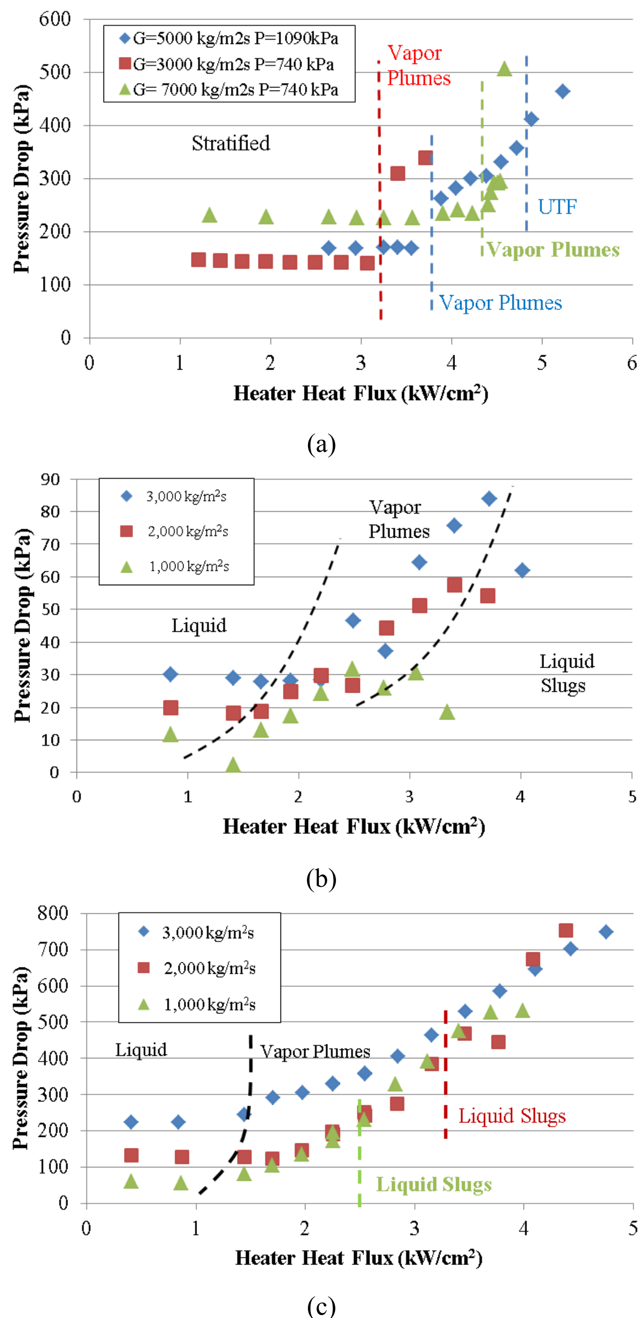

Fig. 14 Pressure Drop vs Heat Flux (a) Gen 1 Device (b) Gen 2 device at 820 kPa system pressure (downstream of microgap) (c) Gen 3 Device at 820 kPa system pressure (downstream of microgap).

Pressure drop in Gen 2 devices is constant for a given mass flux in the single phase flow regime, as expected, and steadily increases with heat addition in the vapor slug boiling domain (Fig 10-a) due to an increased acceleration between phases and viscous losses. The pressure drop reaches a maximum at the point where the boiling regime transitions to liquid slugs as shown in Fig 14-b. As the liquid slug boiling proceeds, the pressure drop decreases with increasing dryout in the microgap. Since outlet pressure is fixed at system pressure, the decrease in pressure drop is a result of a decrease in inlet pressure. Local dryout in the microgap and subsequent transition to liquid slug regime occur when fluid in the inlet

plenum boils. In Gen 2 and Gen3 devices, inlet pressure is recorded in the inlet plenum via pressure tap located in an immediate vicinity of gap entry, as shown in Fig 2. As a result, when fluid boils in the inlet plenum, the pressure recorded does not correspond to the actual fluid pressure at the inlet, but is equal to the saturation pressure at the temperature where the pressure transducing element is located (being further away from the microgap and near the contact with environment, it is always a measure of coolant saturation pressure near ambient temperature). Thus, this has the unintended effect of distorting actual pressure drop when fluid boils in the inlet plenum. The impact of this pressure distortion only affects the data points in the liquid slug/film regimes when the refrigerant vapor is in the inlet plenum. One would expect that the true pressure drop would continue to increase as observed in the Gen 1 device, which had no issues with location of pressure taps.

Boiling pressure drops in Gen 2 devices are significantly smaller in magnitude than those of Gen 1 devices at the same mass fluxes because the microgap height is twice as tall as the Gen 1 device (10 μm vs 5 μm). The pressure drop is higher in the Gen 1 device for the same heat and mass flux because there is a larger vapor content (higher quality) in the smaller gap height than in the larger one due to lower coolant volumetric flow rate in the smaller gap devices at the same mass flux conditions; as a result pressure drop is increased by the acceleration between phases and viscous losses. Alum [2] observed a similar occurrence where microgaps of decreasing height showed substantially larger pressure drop for the same mass fluxes. The Gen 3 device followed the same pressure drop trends as the Gen 2 device in the vapor slug flow regime; however, the pressure drop in the Gen 3 device did not decrease at the transition to liquid slug boiling. The pressure drop never decreased at the liquid slug regime because there was no boiling in the inlet plenum, and therefore the artifact of pressure reading at inlet taps filled with vapor condensed at the environmental temperature was avoided. Note that pressure drop for the 1,000 kg/m^{2}s case exceeds that of 2,000kg/m^{2}s case in liquid slug boiling because the transition to the liquid slug regime occurred at a lower heat flux for the lower mass flux, and therefore the vapor content is higher at the same heat flux, with corresponding increase in the acceleration and viscous pressure drops despite the lower mass flux.

SUMMARY & CONCLUSIONS

Three dedicated hotspot microgap coolers using convective boiling of a high pressure refrigerant R-134a were experimentally characterized in terms of their ability to dissipate ultra-high heat fluxes at application constrained surface temperatures. The heat transfer results, expressed in terms of overall thermal resistances within the devices, were mapped to flow regimes using high resolution optical visualization. All devices showed ability to dissipate ultra-high heat fluxes, up to 4 kW/cm^2 at the heater surface. Gen 1 devices with 5 μm gap height and no fins performed best in the ultra-thin film boiling regime with thermal resistances as low as ~0.045 cm^2-K/W. Conduction heat spreading in Gen 1 devices was reduced in Gen2 and Gen 3 devices by introducing air isolation trenches around the heaters. Gen 2 devices with 10 μm gap and no fins showed a decreasing thermal resistance in the vapor plume regime and an increasing thermal resistance in the liquid slug regime due to reduced wetting of the heated surface. At mass fluxes below 3000 kg/m^{2}s local dryout occurred in the liquid slug flow regime without an efficient thin film boiling regime that was observed at higher mass fluxes. Gen 3 devices, with a dense array of pin fins in a 10 um gap height, also showed decreasing thermal resistance in the vapor plume boiling regime. Thermal resistances increased in the liquid slug regime and no liquid film regime was observed, likely due to film disruption by the pins. Gen 3 devices showed only a 3.5% reduction in minimal thermal resistance compared to Gen 2 devices however the minimal resistance was reached at a significantly higher heat flux for high mass flux tests.

Pressure drop increased with onset of vapor slug boiling in the microgap for all devices. Flow instabilities observed in these devices were minimal and included infrequent flow reversals in the outlet plenum, boiling hysteresis in Gen 1 device, and vapor slug regime flash boiling in Gen 2 devices before transition to liquid slug regime.

ACKNOWELDGEMENTS

The Defense Advanced Research Projects Agency (DARPA) IceCool Fundamentals Program (Award No. HR0011-13-2-0008) provided financial support for this work.

REFERENCES

[1] Hamann, H. F., Weger, A., Lacey, J. A., Hu, Z., Bose, P., Cohen, E., and Wakil, J., Hotspot-limited microprocessors: Direct temperature and power distribution measurements. *Solid-State Circuits, IEEE Journal of*,*42*(1), 56-65 (2007).

[2] Alam, T., Lee, P. S., Yap, C. R., and Jin, L., Experimental investigation of local flow boiling heat transfer and pressure drop characteristics in microgap channel. *International Journal of Multiphase Flow*, 42, 164-174 (2012).

[3] Harirchian, T., and Garimella, S.V., Effects of channel dimension, heat flux, and mass flux on flow boiling regimes in microchannels, *International Journal of Multiphase Flow*, 35, 349-62 (2009).

[4] Alam, T., Lee, P.S., Yap, C.R., Jin, L., Balasubramanian, K., Experimental investigation and flow visualization to determine the optimum dimension range of microgap heat sinks, *International Journal of Heat and Mass Transfer,* 55, 7623-34 (2012).

[5] Khrishnamurthy, S., and Peles, Y., Flow boiling of water in a circular staggered micro-pin fin heat sink, *International Journal of Heat and Mass Transfer*, 51, 1349-64 (2008).

[6] Koşar, A., and Peles, Y., Boiling heat transfer in a hydrofoil-based micro pin fin heat sink. *International Journal of Heat and Mass Transfer*, 50(5), 1018-1034 (2007).

[7] Muwanga, R., I. Hassan, and R. MacDonald. Characteristics of flow boiling oscillations in silicon microchannel heat sinks. *ASME Journal of Heat Transfer,* 129(10), 1341-1351 (2007).

[8] Alam, T., Lee, P. S., Yap, C. R., and Jin, L., A comparative study of flow boiling heat transfer and pressure drop characteristics in microgap and microchannel heat sink and an evaluation of microgap heat sink for hotspot mitigation. *International Journal of Heat and Mass Transfer*, 58(1), 335-347 (2013).

[9] Kottke, P. A., Yun, T. M., Green, C., Joshi, Y. K. and Fedorov, A. G., Two-phase convective cooling for ultra-high power dissipation in microprocessors. *ASME Journal of Heat Transfer*, 138 (1), 011501-011507 (2015).

[10] Bar-Cohen, A., Sheehan, J. R., and Rahim, E., Two-phase thermal transport in microgap channels—theory, experimental results, and predictive relations. *Microgravity Science and Technology*, 24(1), 1-15 (2012).

[11] Bar-Cohen, A., and Rahim, E., Modeling and prediction of two-phase microgap channel heat transfer characteristics. *Heat Transfer Engineering*, 30(8), 601-625 (2009).

[12] Kabov, O. A., Zaitsev, D. V., Cheverda, V. V., and Bar-Cohen, A., Evaporation and flow dynamics of thin, shear-driven liquid films in microgap channels. *Experimental Thermal and Fluid Science*, 35(5), 825-831 (2011).

[13] Gatapova, E. Y., and Kabov, O. A., Shear-driven flows of locally heated liquid films. *International Journal of Heat and Mass Transfer*, 51(19), 4797-4810 (2008).

[14] Kabov, O. A., Lyulin, Y. V., Marchuk, I. V., and Zaitsev, D. V., Locally heated shear-driven liquid films in microchannels and minichannels. *International Journal of Heat and Fluid Flow*, 28(1), 103-112 (2007).

[15] Kakaç, S., Vasiliev, L. L., Bayazitoglu, Y., and Yener, Y. (Eds.). (2006).*Microscale Heat Transfer-Fundamentals and Applications: Proceedings of the NATO Advanced Study Institute on Microscale Heat Transfer-Fundamentals and Applications in Biological and Microelectromechanical Systems,* Cesme-Izmir, Turkey, 18-30 July, 2004 (Vol. 193). Springer Science & Business Media.